Large-Scale Sea Level Response to Atmospheric Forcing along the West Coast of North America, Summer 1973

GEORGE R. HALLIWELL, JR. AND J. S. ALLEN

College of Oceanography, Oregon State University, Corvallis, OR 97331

(Manuscript received 19 October 1983, in final form 21 February 1984)

ABSTRACT

Along the west coast of North America, the response of sea level to fluctuations in alongshore wind stress at large alongshore scales (>1000 km) accounted for a substantial fraction of the total sea level variance during summer 1973. Space–time contour plots of sea level and alongshore stress show that the response of sea level to poleward propagating wind stress events was generally stronger than the response to equatorward propagating events. Atmospheric forcing was most effective in two regions along the coast, with relatively strong forcing and response along northern California and Oregon, and somewhat weaker forcing and response along northern Baja California. The forced fluctuations in sea level propagated poleward away from these forcing regions, causing local sea level to be most correlated with alongshore wind stress earlier in time and at a distant equatorward location. Along the southern and central California coast, fluctuations in sea level were partly forced along northern Baja California, although some of the energy may have entered the domain from the south. Poleward of Crescent City, fluctuations in sea level were dominated by the response to alongshore stress in the northern forcing region, and were therefore poorly correlated with sea level to the south. Most of the sea level energy was contained in two frequency domain modes representing the northern and southern fluctuations in sea level. The southern mode had proportionally more energy than the northern mode at a frequency of 0.043 cpd, while the opposite was true for frequencies between 0.086 and 0.22 cpd. Sea level apparently responded more effectively in frequency bands where fluctuations in wind stress propagated poleward and acted over a longer alongshore distance. Along the British Columbia coast, local atmospheric forcing was relatively ineffective, and fluctuations in sea level were apparently dominated by free wave energy propagating poleward from the northern forcing region. Predictions of sea level response made from simple theory of wind-forced coastal-trapped waves were similar to the observed response, and accounted for up to 70% of the total variance along Oregon and Washington, poleward of the northern forcing region.

1. Introduction

Theoretical models for wind-driven shelf currents (e.g., Gill and Schumann, 1974) illustrate the nature of the response to atmospheric forcing at large alongshore scales; i.e., at scales much larger than the width of the continental margin. In these models, the alongshore component of wind stress is the dominant forcing mechanism. Since midlatitude atmospheric systems typically have spatial scales of several hundred to several thousand kilometers and time scales of 2 days to about 2 weeks, large-scale perturbations driven by coastal atmospheric forcing should be an important component of the variability of coastal currents at these time scales. In addition, a continental margin theoretically acts as a waveguide for subinertial frequency coastal-trapped waves, which are nondispersive for large alongshore scales and propagate poleward along eastern boundaries. Thus, large-scale current fluctuations at a given location along a continental margin can be partly or totally forced at distant locations, and the possibility of resonant forcing exists if a wind stress perturbation propagates along the coast at the free wave velocity of a coastal-trapped wave mode. These theoretical results indicate the importance of resolving large-scale forcing and response in order to understand the behavior of currents measured at any particular geographical location during shelf dynamics field experiments.

A primary objective of the Coastal Ocean Dynamics Experiment (CODE) is to determine the dynamics of wind-driven coastal currents along a 100 km segment of the California coast centered near 38°42'N (Fig. 1) during two time intervals: April through August 1981

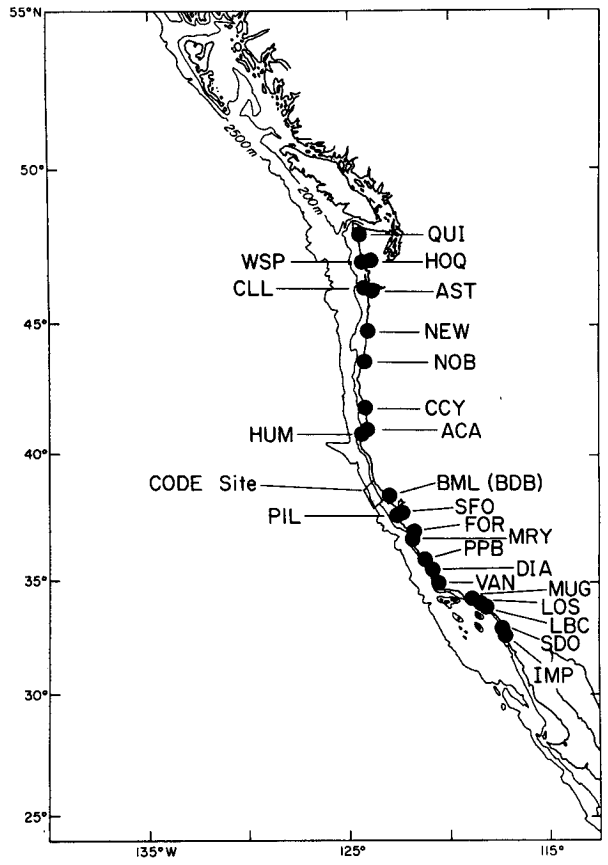

FIG. 1. Coastal meteorological stations available during summer 1973. If more than one station is present at a given location, the other station abbreviations are shown in parentheses. The location of the CODE experimental site, centered near latitude 38°41'N, is shown. Station information is summarized in Table 1.

(CODE-I) and April through August 1982 (CODE-II) (Allen *et al.*, 1983). As part of CODE, a large-scale study has been designed to determine the nature of the large-scale forcing and response along a 3600 km section of the coast from central Baja California to northern British Columbia (26–54°N) for the three-year interval April 1980 through March 1983, and to determine the influence of large-scale processes on currents observed at the CODE site. In the large-scale study, atmospheric forcing is represented by wind and pressure measured at continental United States and Canadian coastal stations and buoys, and by alongshore wind stress calculated from Fleet Numerical Oceanography Center (FNOC) atmospheric pressure analyses. Coastal sea level measurements from all available continental United States and Canadian stations are used to represent the response of coastal currents, based on the generally high correlation of sea level and alongshore currents established by previous observations (e.g., Smith, 1974). The use of sea level as the response variable in place of currents is discussed in Appendix A.

Prior to analyzing the large-scale response during CODE, it was deemed useful to perform a similar study for the United States west coast during the summer of 1973 to test the assumptions and analysis procedures. Summer 1973 was chosen because the Coastal Upwelling Experiment (CUE-II) was performed off Oregon (near 45°N) during July and August 1973, providing a well studied set of current measurements at one location along the coast. Also, limited aspects of the large-scale response during that time interval have been studied by Wang and Mooers (1977). Our more extensive analyses of data spanning longer space and time scales enable us to present many new results concerning the large-scale nature of the atmospheric forcing and response along the west coast of North America during summer 1973. Our primary purpose in this paper is to characterize statistically the nature and interrelationship of the forcing and response independent of any dynamical models (Sections 4–6). We then briefly show that a simple linear model of wind-driven coastal-trapped waves qualitatively predicts the observed statistical relationship between the forcing and response (Section 7).

2. The data set

In the following analyses, we use a right-handed curvilinear coordinate system with y parallel to the coast, increasing in the poleward direction, and x normal to the coast, increasing onshore. The alongshore direction at a given location along the coast is estimated by visually smoothing the coast over a sufficiently long segment to eliminate the irregularities due to small headlands and bays (typically 10 to 20 km). The origin is on the coast at the latitude of the central line of the CODE experiment (38°42'N). The time variable is t.

a. Atmospheric forcing

Atmospheric forcing is represented by measured data at selected coastal meteorological stations (Table 1, Fig. 1) and by analyzed fields obtained from FNOC (Bakun, 1973) that have been interpolated to coastal points of the CODE analysis grid (Table 2, Fig. 2). The 20 coastal CODE grid points are separated by 180 km,[1] with grid point 7 located at the origin of the coordinate system, $y = 0$. Surface atmospheric pressure (p) and wind components along the east–west and north–south axes (u, v) are obtained from the coastal

[1] This spacing is used because analyzed variables from the National Weather Service LFM-II forecast model are available on a grid with similar spacing at middle latitudes. LFM data are not used for summer 1973 because of substantial gaps.

TABLE 1. Meteorological station information and basic statistics of measured τ.

Station	Symbol	Latitude (deg min)	Longitude (deg min)	y^* (km)	Geographical coast† orientation (deg)	Variables		Stations selected for analyses	Measured τ statistics (dyn cm^{-2})	
						p	Wind		Mean	Std dev
Quillayute, WA	QUI	47 57 N	123 32 W	1055	110	Yes	Yes	×	0.01	0.08
Hoquiam, WA	HOQ	46 58	123 56	942	95	Yes	Yes			
Westport, WA	WSP	46 55	124 06	935	95	No	Yes			
Columbia River Lightship	CLL	46 11	124 11	854	90	Yes	No	×	0.03	0.56
Astoria, OR	AST	46 09	123 53	850	90	Yes	Yes			
Newport, OR	NEW	44 38	124 03	683	82	Yes	Yes	×	−0.05	0.53
North Bend, OR	NOB	43 25	124 15	547	73	Yes	Yes	×	−0.02	0.37
Crescent City, CA	CCY	41 47	124 14	362	103	No	Yes	×	−0.09	0.34
Arcata, CA	ACA	40 59	124 06	270	75	No	Yes			
Humboldt Bay, CA	HUM	40 46	124 14	246	75	No	Yes	×	−0.12	0.07
Bodega Marine Lab, CA	BML	38 20	123 04	−46	133	No	Yes	×	−0.23	0.35
Bodega Bay, CA	BDB	38 19	123 04	−48	133	No	Yes			
San Francisco, CA	SFO	37 37	122 23	−142	105	Yes	No			
Pillar Point, CA	PIL	37 30	122 30	−156	105	No	Yes	×	−0.15	0.34
Fort Ord, CA	FOR	36 41	121 46	−264	110	No	Yes			
Monterey, CA	MRY	36 35	121 51	−278	110	No	Yes			
Point Piedras Blancas, CA	PPB	35 40	121 17	−401	130	No	Yes			
Diablo Canyon, CA	DIA	35 14	120 50	−464	120	No	Yes	×	−0.39	0.40
Vandenberg AFB, CA	VAN	34 43	120 52	−528	90	No	Yes			
Point Mugu, CA	MUG	34 07	119 07	−678	155	Yes	Yes	×	−0.03	0.05
Los Angeles, CA	LOS	33 56	118 24	−757	150	Yes	Yes			
Long Beach, CA	LBC	33 49	118 09	−785	150	Yes	Yes	×	0	0.04
San Diego, CA	SDO	32 44	117 10	−936	105	Yes	Yes	×	−0.02	0.12
Imperial Beach, CA	IMP	32 34	117 07	−954	105	Yes	Yes			

* The CODE central line (38°42′N) is at y = 0 km.
† Geographical orientations are 0 degrees for due east, 90 degrees for due north, etc.

TABLE 2. Coastal points of the CODE analysis grid and basic statistics of calculated τ.

Grid point	Latitude (deg min)	Longitude (deg min)	y^* (km)	Geographical coast† orientation (deg)	Calculated τ statistics (dyn cm^{-2})	
					Mean	Std dev
16	52 10 N	128 19 W	1620	115	0.04	0.40
15	50 32	127 13	1440	100	0.08	0.47
14	49 23	126 06	1260	125	−0.07	0.39
13	48 11	124 42	1080	115	−0.09	0.27
12	46 36	124 05	900	95	−0.12	0.28
11	44 58	124 03	720	85	−0.23	0.42
10	43 12	124 20	540	73	−0.35	0.58
9	41 46	124 12	360	103	−0.82	0.90
8	40 12	124 18	180	130	−1.20	1.12
7	38 41	123 27	0	133	−1.09	0.85
6	37 18	122 24	−180	102	−0.50	0.35
5	35 59	121 31	−360	128	−0.74	0.42
4	34 35	120 39	−540	90	−0.72	0.43
3	34 01	118 53	−720	150	−0.94	0.49
2	33 00	117 21	−900	110	−0.45	0.22
1	31 27	116 44	−1080	110	−0.42	0.22
35	30 00	115 54	−1260	115	−0.33	0.23
34	28 47	114 51	−1440	130	−0.35	0.24
33	27 20	113 52	−1620	130	−0.24	0.19
32	26 07	112 40	−1800	130	−0.18	0.16

* The CODE central line is located at y = 0 km.
† Geographical orientations are 0 deg for due east, 90 deg for due north, etc.

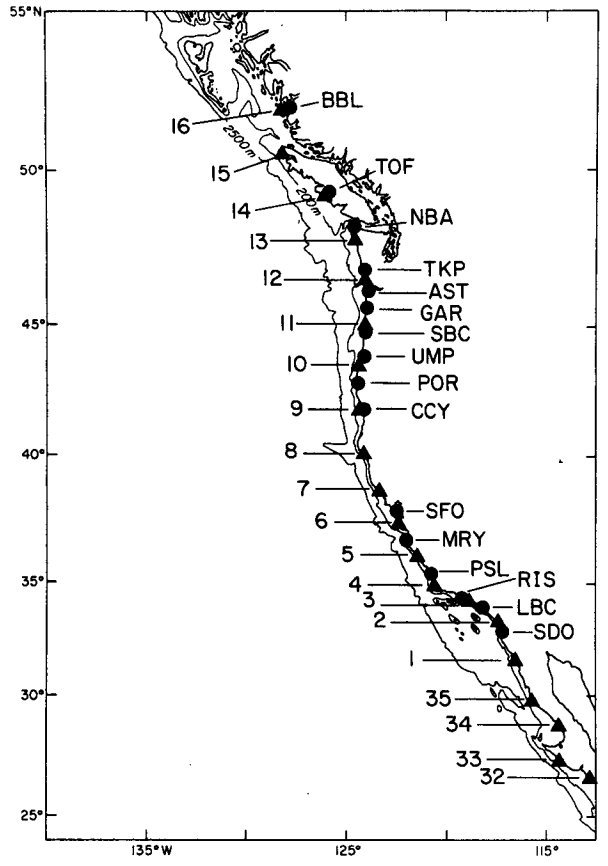

FIG. 2. Coastal points of the CODE large-scale analysis grid (triangles) and sea level stations (circles). Grid points 17 through 31, most of which are located offshore, are not shown. Grid point information is summarized in Table 2, and the sea level station information is summarized in Table 3.

meteorological stations. Analyzed fields of p, u and v are obtained at the CODE grid points. The variables obtained from FNOC will hereafter be referred to as calculated variables. Alongshore positions (y coordinates) of all meteorological stations and grid points are presented in Tables 1 and 2.

Calculated winds are obtained from the six-hourly FNOC pressure fields by the methods described by Bakun (1973). Pressures are interpolated to grid points separated by three degrees of latitude and longitude, resulting in a north–south spatial resolution of about 300 km at all latitudes, and an east–west resolution of about 240 km at the latitude of the CODE site. Geostrophic winds are calculated from these gridded pressures. To obtain estimates of surface winds, a simple boundary layer correction is applied by reducing wind speed by 30% and rotating wind vectors 15 degrees counterclockwise (Bakun, 1973).

The measured meteorological data are obtained from several sources at sampling rates between one and six hours. The data sources and editorial procedures are discussed by Halliwell and Allen (1983, 1984). After editing, the following major steps are performed on all measured and calculated time series: 1) gaps less than 24 h in length within the time series are filled by linear interpolation; 2) measured wind speed is adjusted to an anemometer height of 10 m assuming a logarithmic velocity profile (neutral stability) (calculated winds are assumed to represent 10 m winds); and 3) time series are low-pass filtered using a Cosine-Lanzcos filter with a 40 h cutoff and subsampled to 6 h when necessary (Pittock *et al.*, 1982). The filtered time series start at 0000 PST 4 June and end at 0600 PST 27 September 1973 and have a sampling rate of 6 h. We compute wind stress for both calculated and measured winds prior to filtering by using the bulk aerodynamic equation with a drag coefficient given by (Large and Pond, 1981):

$$10^3 C_d = \begin{cases} 1.2, & |\mathbf{V}_{10}| \leq 11 \text{ m s}^{-1} \\ 0.49 + 0.065|\mathbf{V}_{10}|, & |\mathbf{V}_{10}| > 11 \text{ m s}^{-1}. \end{cases}$$

The axes are then rotated to compute stress components in the curvilinear coordinate system (Section 3). The alongshore component of stress is used as a forcing function, and hereafter referred to as τ.

b. *Adjusted coastal sea level*

Coastal sea level data are obtained from the National Ocean Survey and the Canadian Marine Environment Service (Table 3). These data are checked for datum shifts (Pittock *et al.*, 1982), then subjected to essentially the same editorial procedure as meteorological data (Halliwell and Allen, 1983). Adjusted sea level (ζ), corresponding to pressure beneath the sea surface, is formed by adding the equivalent of atmospheric pressure to the sea level data (in cm). The p time series used in this adjustment are listed in Table 3. In cases where p is not available within about 50 km of the sea level station, it is estimated by linear interpolation using the two nearest p stations of the same type (i.e., both calculated or both measured), one equatorward of, and one poleward of, the ζ station. The mean values of ζ are then removed. The start and end times are the same as for the meteorological data. Time series of ζ are linearly interpolated to the coastal CODE analysis grid (points 2–16) with allowances made for time lags between the input time series of measured ζ caused by propagating disturbances. These lags are objectively determined using lagged cross-correlation analysis. Details of the interpolation procedure are presented by Halliwell and Allen (1983).

3. Comparison of calculated and measured wind

Calculated winds form an attractive data set for analysis because they are spatially complete, available on a regular grid, and derived by uniform procedures

TABLE 3. Coastal sea level station information and standard deviation of ζ.

Station	Symbol	Latitude (deg min)	Longitude (deg min)	y (km)	Stations or grid point numbers for atmospheric pressure used in forming adjusted sea level	Standard deviation of ζ (cm)
Bella Bella, BC	BBL	52 10 N	128 08 W	1608	CG16	5.08
Tofino, BC	TOF	49 09	125 55	1232	CG14	4.83
Neah Bay, WA	NBA	48 22	124 37	1100	CG13	5.30
Toke Point, WA	TKP	46 42	123 58	911	CG12	7.57
Astoria, OR	AST	46 10	123 46	852	Astoria	6.45
Garibaldi, OR	GAR	45 25	123 55	770	Astoria-Newport*	6.99
South Beach, OR	SBC	44 38	124 03	678	Newport	5.80
Umpqua River, OR	UMP	43 42	124 10	579	North Bend	5.94
Port Orford, OR	POR	42 45	124 30	469	North Bend	5.40
Crescent City, CA	CCY	41 45	124 11	359	CG9	4.61
San Francisco, CA	SFO	37 48	122 28	−126	San Francisco	3.87
Monterey, CA	MRY	36 36	121 53	−276	CG5–CG6*	2.84
Port San Luis, CA	PSL	35 10	120 45	−473	Calculated**	3.51
Rincon Island, CA	RIS	34 21	119 27	−650	Pt. Mugu	3.44
Long Beach, CA	LBC	33 45	118 13	−785	Long Beach	3.54
San Diego, CA	SDO	32 45	117 10	−938	San Diego	3.44

* Linearly interpolated.
** Calculated pressure was also obtained at Port San Luis.

TABLE 4. Summary of the two comparisons of calculated and measured vector winds: 1) the inner correlation and phase, and 2) comparison of both wind sets to sea level. Since integral correlation time scales vary for different time series, statistically significant correlations range between 0.31 and 0.38 to a 95% level of confidence.

Inner correlation and phase (calculated minus measured)				Geographical wind orientations most correlated with ζ			
Grid point	Measurement station	Correlation	Phase (deg)	Measurement station or grid point	ζ station	Orientation (deg)†	Correlation
2	IMP	0.77	60	1	SDO	74	0.42
2	SDO	0.69	53	5	MRY	65	0.57
3	LBC	0.65	59	6	SFO	37	0.55
3	LOS	0.86	76	PIL	SFO	85	0.59
3	MUG	0.74	58	7	CCY	48	0.56
4	VAN	0.88	−11	BDB	CCY	115	0.54
4	DIA	0.88	12	BML	CCY	115	0.54
5	PPB	0.48	19	8	CCY	22	0.58
5	MRY	0.86	50	HUM	CCY	92	0.55
6	MRY	0.85	59	9	CCY	35	0.57
6	FOR	0.90	70	ARC	CCY	89	0.54
6	PIL	0.68	41	CCY	CCY	103	0.59
7	BDB	0.79	40	10	UMP	42	0.79
7	BML	0.80	47	NOB	UMP	66	0.71
8	HUM	0.70	68	11	SBC	44	0.79
9	ARC	0.58	57	NEW	SBC	62	0.74
9	CCY	0.60	67	12	AST	45	0.78
10	NOB	0.89	19	AST	AST	68	0.50
11	NEW	0.75	23	CLL	AST	70	0.51
12	AST	0.66	56	WSP	AST	86	0.47
12	CLL	0.83	35	13	NBA	73	0.42
12	WSP	0.80	45				
12	HOQ	0.87	60				
13	QUI	0.76	57				

† Geographical orientations are 0 deg for due east, 90 deg for due north, etc.

over that grid. In contrast, available coastal measured winds have irregular spacing alongshore and are of variable quality because of differences in local topography, instrument location, etc. For these reasons, calculated winds are used extensively in the following analyses. A thorough comparison between calculated and measured winds is given by Halliwell and Allen (1984). Several aspects of the comparison are important for the present study and are discussed here. We first compare fluctuations in calculated vector winds to fluctuations in measured vector winds, then quantify an additional rotation that must be performed on the calculated winds to bring their fluctuations into alignment with those of the measured winds. In Appendix B, we compare some of the analyses in Section 6 performed using calculated τ with similar analyses using measured τ and show that reliable results are obtainable with calculated τ.

At each grid point, the inner correlation and phase between calculated vector winds and all measured vector winds within 90 km (Table 4) show that the winds are rather well correlated in most cases, being greater than 0.7 for 17 out of the 24 cases. The inner phase gives the difference in angular orientation between the fluctuations that is weighted by the amplitude of the instantaneous vectors (Kundu, 1976). All inner phases except one are positive, and the largest is 76°. Positive inner phase means that calculated vector winds must be rotated counterclockwise to bring their fluctuations into alignment with the measured winds. The inner phase varies along the coast, being relatively small (<25°) near Point Conception (grid point 4) and along the Oregon coast (grid points 10 and 11), and larger elsewhere.

Because of the possible influence of local topography on measured winds, we cannot assume that they accurately represent the orientation of wind fluctuations over the shelf. Therefore, we cannot assume that the inner phase between calculated and measured winds provides an accurate estimate of the rotation error in calculated winds. An independent estimate of the rotation error is obtained by comparing the relation of both calculated and measured vector winds to ζ. The orientations of the components of these winds most correlated with ζ are estimated by regressing sea level on wind components in the time domain, then using the regression coefficients to calculate the orientations (Garrett and Toulany, 1982). The results are presented in Table 4 for all measurement stations and grid points where the vector winds explain a statistically significant fraction of the ζ variance to 95% confidence. The maximum-correlation orientations for the calculated winds are typically smaller than (rotated clockwise from) the orientations of the measured winds. This misalignment becomes very clear by inspecting the basic statistics of the difference between these computed orientations and the corresponding geographical alongshore orientations. For the eleven measured wind orientations listed in Table 4 this difference is $-9° \pm 14°$, and for the ten calculated wind orientations it is $-54° \pm 17°$. Thus, it is roughly the geographical alongshore component of measured wind that is most correlated with sea level, but a component of calculated wind that is, on average, more than 50° clockwise from the geographical alongshore orientation is most correlated with ζ. We therefore conclude that local topography does not seriously change the orientation of the fluctuations in measured wind and that the inner phase provides a reasonably good estimate of the rotation error. Calculated winds (and wind stress) must therefore be rotated counterclockwise to best represent the true coastal winds.

We emphasize that this correction may only apply to winds measured at or near the coast. The 15° counterclockwise rotation of the calculated winds performed during the boundary layer correction may be sufficient to best represent the true surface wind over the open ocean, but the marine coastal boundary layer is influenced by other factors, such as the presence of coastal mountains, surface horizontal temperature gradients, and diurnal wind fluctuations. These additional influences may substantially affect the veering of the wind vertically through the marine boundary layer near the coast and change the rotation required to align the calculated winds with the measured winds at the surface. Our results indicate that along most of the coast, a 15° counterclockwise rotation is insufficient to correct for wind veering in the coastal marine boundary layer. Similar misalignments between calculated winds and coastal measured winds are also observed in the CODE large-scale data set (Halliwell and Allen, 1984). Also, Thomson (1983), in a comparison of calculated winds to measured winds from two meteorological buoys along the British Columbia coast during two summer seasons 1979 and 1980, found that calculated wind vectors had to be rotated an additional 20° counterclockwise to be aligned properly with the measured wind.

The correlation coefficients between these components of calculated and measured winds and the nearby ζ measurements are also presented in Table 4. The calculated winds are slightly better correlated with ζ than the measured winds along most of the coast between grid points 5 and 12. The measured winds may be substantially affected by factors such as small-scale wind fluctuations and local topography. Calculated winds apparently represent the large-scale wind fluctuations that drive oceanic response with enough accuracy to be an adequate forcing function for the purpose of this study. This conclusion is supported by the analyses presented in Appendix B.

Since the rotation correction is apparently a function

TABLE 5. Computation of the alongshore component of calculated wind stress. The average inner phase difference and the average difference between wind orientations most correlated with sea level are computed from the data in Table 4.

	Difference (calculated minus measured) between inner phases		Average difference between wind orientations most correlated with ζ (calculated minus measured)		Computation of the "alongshore" calculated wind stress	
Grid point	Average (deg)	Number of wind measurement stations	Difference in angles (deg)	Number of wind measurement stations	Geographical orientation of the coast (deg)†	Estimated correction angle to align calculated wind with the true wind at the coast
1	—	0	—	0	110	60
2	57	2	—	0	110	60
3	64	3	—	0	150	60
4	0	2	—	0	90	0
5	35	2	—	0	128	38
6	57	3	48	1	102	52
7	44	2	67	2	133	58
8	68	1	70	1	130	70
9	62	2	61	2	103	58
10	19	1	24	1	73	18
11	23	1	18	1	85	20
12	49	4	30	3	95	40
13	57	1	—	0	115	55
14	—	0	—	0	125	55
15	—	0	—	0	100	55
16	—	0	—	0	115	55

† Geographical orientations are 0 degrees for due east, 90 degrees for due north.

of alongshore position, we estimate a separate correction at each grid point. We use both the inner phase and the differences in wind orientation most correlated with ζ to estimate these corrections, since very few estimates of the inner phase exist at each grid point and therefore they alone cannot provide a good estimate of the rotation correction. Average values of the differences between measured and calculated winds in inner phase and in the wind orientation most correlated with ζ are presented in Table 5. At grid points 6 through 12, where both could be computed, they have similar values, which increases our confidence that they both approximately measure the misalignment between fluctuations in calculated and measured winds.

We therefore estimate τ in the following manner: For measured τ, we simply compute the alongshore component of the measured vector stress. For calculated τ, we first rotate the calculated vector stress at each grid point by an amount determined by averages of the two differences presented in Table 5 to correct for the misalignments. We then compute calculated τ in the same manner as measured τ. Estimates of the correction angles at each grid point are presented in Table 5. At grid points 2–5 and 13, only the average inner-phase difference could be used to estimate the correction angles. At grid points 1, 14, 15 and 16, there were no statistics upon which to estimate the correction angles. We determine the correction angle for grid point 1 by assuming that it is the same as for grid point 2. Similarly, the correction angles for grid points 14–16 are assumed to be the same as for grid point 13.

For the analyses performed in Appendix B using measured τ, we use a subset of the measured wind stations in Table 1. These stations are selected to be as evenly spaced as possible along the coast, with an effort made to use better-quality winds wherever possible. These stations are marked in Table 1, where the basic statistics of τ are presented. Both the mean and standard deviation of measured τ are substantially smaller than those for calculated τ presented in Table 2. The measured wind statistics also vary irregularly from station to station along the coast while the calculated τ statistics vary smoothly. Apparently, both the mean values of measured τ and the amplitudes of its fluctuations are strongly influenced by factors such as local topography. Therefore, we rely only on the basic statistics of calculated τ in the following analyses.

4. The alongshore-time properties of wind-stress forcing and response

a. Basic statistics of ζ and τ

The dominant feature in the alongshore distribution of the means and standard deviations of τ (Table 2) is that both have large magnitudes at grid point 8, which is located near Cape Mendocino. (Unless otherwise noted, τ will represent calculated τ for the remainder of this paper. Measured variables will always

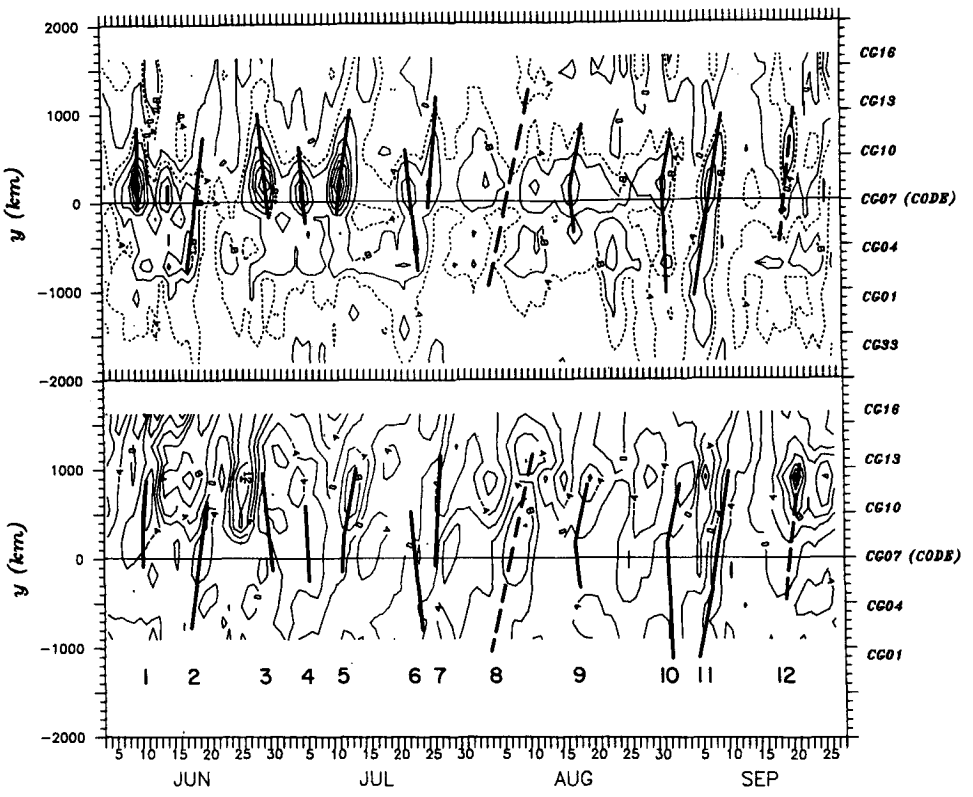

FIG. 3. Space–time contours of (top) daily averaged calculated τ and (bottom) daily averaged demeaned gridded ζ for summer 1973. Twelve τ events are numbered sequentially, and time lines denoting the locations and times of the τ extrema associated with these events are shown in both panels. These time lines are solid for τ minima (maximum equatorward τ) and dashed for τ maxima. The contour intervals for the solid contours are 0.8 dyn cm^{-2} for τ and 4 cm for ζ. Intermediate contours are dashed.

be prefixed by the word measured.) The mean at this point is equatorward, as it is everywhere south of northern Vancouver Island. The standard deviation at this point is four to five times larger than it is along the coasts of northern Baja California, southern California, and Washington. Smaller relative maxima in the standard deviation exist near Point Conception (grid point 4) and along the northern British Columbia coast. In contrast, the largest ζ standard deviation (Table 3) occurs along the Washington coast, with minima located along the coasts of central California and southern British Columbia. In general, maxima and minima of ζ standard deviations are displaced poleward of corresponding maxima and minima of τ standard deviations, suggesting a poleward shift in the response of ζ to τ.

b. *Alongshore-time contour plots of ζ and τ*

Contours of daily averages of τ and gridded ζ are presented in Fig. 3. Fluctuations of τ are largest near $y = 180$ km, the latitude of Cape Mendocino. Twelve τ events,[2] some poleward (positive τ) extrema and some equatorward (negative τ) extrema, are labeled in Fig. 3. Time lines of these events, defined here as the lines in the y–t plane tracing the location of the τ extrema as a function of time, are indicated by solid lines for equatorward extrema and dashed lines for poleward extrema. For most events, the τ extrema do not occur simultaneously along the coast, but propagate poleward or equatorward as indicated by the slopes of the time lines, which provide estimates of propagation speeds.

The τ event time lines are reproduced on the ζ contour chart (Fig. 3). The maximum ζ response is characteristically located poleward of, and later in time than, the τ event. In general, ζ appears to respond more effectively to poleward propagating τ extrema.

[2] We use the term "event" to denote these 12 specific wind stress extrema, although they are not completely independent in time from other extrema.

The ζ response to the poleward propagating events in Fig. 3 [2, 5, 7, 8, 9 (northern part), 10 (northern part), 11 and 12] is substantially larger than the response to the equatorward propagating events [3, 4, 6, 9 (southern part), and 10 (southern part)]. A ζ response of intermediate amplitude occurs for event 1, for which the τ extremum is in-phase along the coast. To assess the ζ-response to τ better, we examine events 4, 5 and 11 in more detail in Section 7 and compare them with an idealized theoretical model response of ζ to the observed τ field.

It can be seen qualitatively from Fig. 3 that both the τ and ζ fields are dominated by large-scale fluctuations with wavelengths greater than 1000 km. This is supported quantitatively by wavenumber autospectra of ζ and τ (four-month ensemble averages of six-hourly wavenumber spectra) plotted in Fig. 4. Most of the energy in both ζ and τ exists in fluctuations with wavelengths greater than 1000 km. Only a very small fraction (about 0.03) of ζ variance exists at wavelengths smaller than the FNOC Nyquist wavelength for τ of about 600 km. Since we focus only on these dominant large-scale fluctuations in this report, the fact that calculated τ does not adequately represent fluctuations with spatial scales less than several hundred kilometers should not lead to serious problems in using it as the wind stress forcing function.

c. *Time-domain EOFs of ζ and τ*

Time-domain EOFs of gridded ζ (Figs. 5 and 6) are calculated to determine the alongshore structure of ζ. Mode 1 (56% of the total variance) essentially represents a northern mode, and mode 2 (23%) a southern mode, indicating that ζ fluctuations poleward of Crescent City (CCY) are poorly correlated with those equatorward of CCY. This discontinuity is very evident in the distribution of the percent variance explained for each mode. This agrees with the results of Osmer and Huyer (1978), who discovered a discontinuity in ζ correlation located beween CCY and Charleston (CHR) during the summers of 1973 through 1975. The EOFs presented here indicate that the boundary between the subdomains is located near CCY during the summer of 1973.

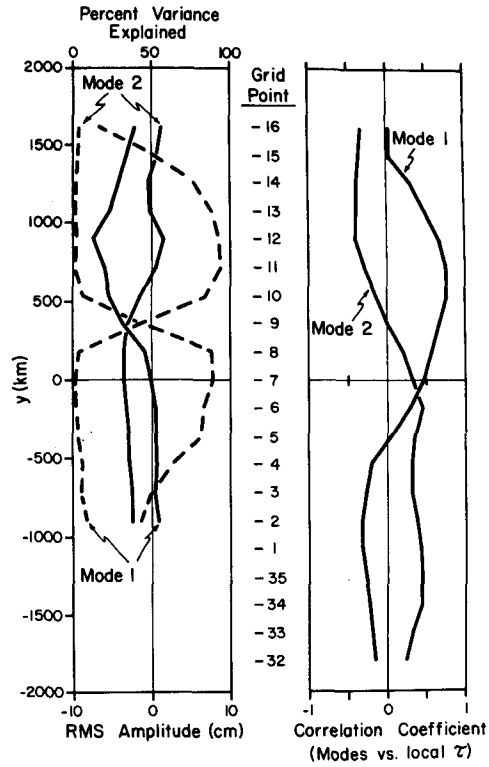

FIG. 5. The two most significant time domain EOFs of gridded ζ: (left) rms amplitudes (solid lines) and percent variance explained (dashed lines); and (right) correlation with local calculated τ that has been lagged by one day to approximately maximize the local correlation. The modes account for 56 and 23% of the total variance, respectively.

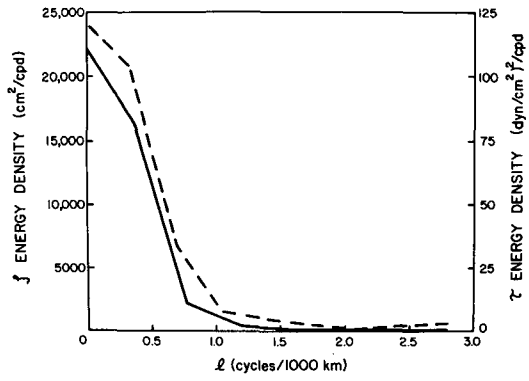

FIG. 4. Wavenumber autospectra of gridded ζ (solid line) and calculated τ (dashed line), ensemble averaged over 4 months from six-hourly autospectra. Based on average integral time scales (Davis, 1976), the ζ spectrum has approximately 30 degrees of freedom, and the τ spectrum has approximately 37 degrees of freedom.

Time-varying amplitudes and their autospectra, plotted in Fig. 6, indicate that the southern mode is relatively more energetic at lower frequencies than the northern mode, with 69% of the southern mode energy and 41% of the northern mode energy existing at frequencies less than 0.043 cycles per day (cpd), and 29% of the southern mode energy and 55% of the northern mode energy existing at frequencies between 0.043 and 0.22 cpd. A time scale equal to, or greater than, four months is also visually evident in the southern mode. Therefore, some of the energy in the southern mode may have originated near the equator as discussed by Enfield and Allen (1980) and Chelton and Davis (1982).

The correlations between these time-varying amplitudes and local τ indicate that the northern mode

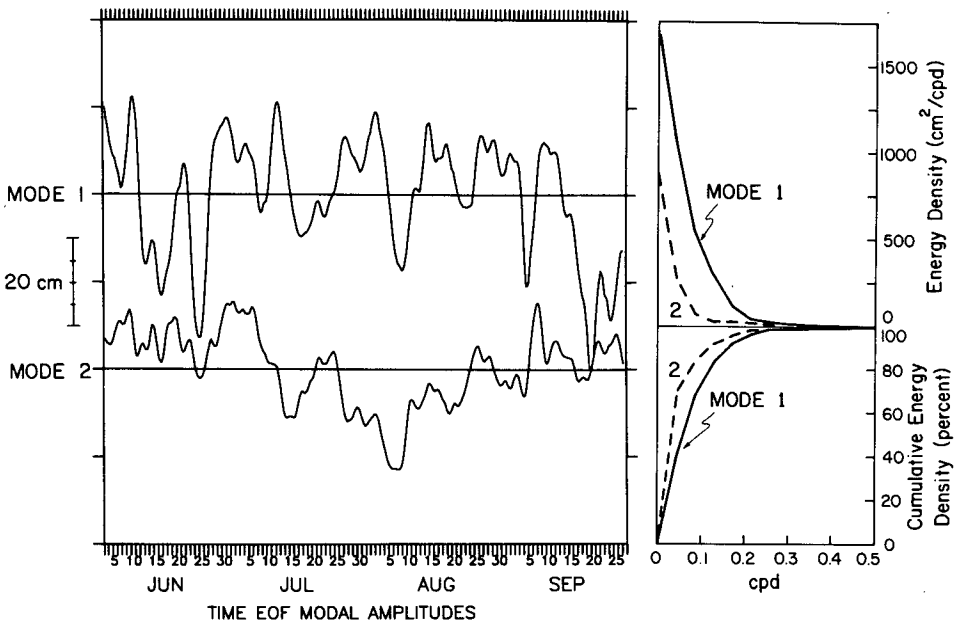

FIG. 6. Time-varying amplitudes of the two most significant EOFs of gridded ζ from Fig. 5 (left) and autospectra of these amplitudes graphed as energy density (right top) and as cumulative energy density in percent (right bottom). The autospectra were computed with a frequency bandwidth of 0.043 cpd, resulting in 10 degrees of freedom.

is strongly related to τ along the coast between Northern California and Washington (Fig. 5). The southern mode is marginally significantly correlated with τ to the south of the CODE site, with two correlation maxima located near $y = -180$ km [between San Francisco (SFO) and Monterey (MRY)] and $y = -1440$ km (northern Baja California). Therefore, the southern ζ mode may be forced in part by wind stress fluctuations. The correlations between the southern mode and local τ change sign poleward of Cape Mendocino and approach marginally significant levels along the Washington and British Columbia coast. This probably occurs because of large-scale correlation patterns in the τ field.

Time domain EOFs of τ are presented in Fig. 7 to characterize the large-scale structure of the τ fluctuations. Mode 1 is dominated by the energetic τ fluctuations near Cape Mendocino, while mode 2 is dominated by large-scale fluctuations with wavelengths of at least 3000 km and a node near Cape Mendocino. Mode 1 explains almost all of the variance at the grid points near Cape Mendocino. Mode 2 explains about half of the variance at the grid points along the Washington coast and along the southern California and Baja California coasts. The northern ζ mode is significantly correlated with both τ modes 1 and 2, with maximum correlation coefficients and time lags for the τ mode of, respectively, (0.63, 1.5 days) and (0.45, 0.75 days). The southern ζ mode is significantly correlated with τ mode 2 only (0.57, 1.5 days). There is no significant correlation between ζ modes 1 and 2 and higher τ modes. The northern ζ mode is apparently primarily forced by the energetic τ fluctuations centered near Cape Mendocino, although there is some contribution from the larger-scale τ fluctuations represented by mode 2. The τ fluctuations that are at least partly responsible for driving the southern ζ mode are apparently part of a large-scale atmospheric oscillation for which we have sampled less than one wavelength in the alongshore direction.

5. The alongshore-frequency properties of wind-stress forcing and response

a. Autospectra

Autospectra of ζ and τ (Fig. 8) are computed at each sea level station or grid point, then contoured as a function of y and frequency. The energy of ζ fluctuations generally increases poleward from the southern end of the domain over all frequencies, reaching a maximum along the southern Washington coast. The energy then decays rapidly poleward through central British Columbia, then slowly increases along the northern British Columbia coast. Relatively energetic fluctuations in ζ also exist for $y \leq -500$ km near 0.4 cpd.

The distribution of ζ and τ energy along the coast shows the poleward displacement of the ζ response to

τ noted in the discussion of basic statistics (Section 4). Fluctuations in τ are most energetic near Cape Mendocino, and smaller alongshore energy maxima exist near Point Conception ($y = -540$ km) and along the northern British Columbia coast over all frequencies. The alongshore energy maximum of ζ is displaced poleward from the τ energy maximum near Cape Mendocino, and is located near the latitude of a τ energy minimum. A ζ energy minimum along the central British Columbia coast is displaced about 400 km poleward of this τ energy minimum.

b. Frequency domain EOFs

The two most significant frequency domain EOFs (Wallace and Dickinson, 1972) of gridded ζ are presented in Fig. 9. For each mode, rms amplitude, percent variance explained (which is 100 times the coherence squared with gridded ζ), and phase lag in hours are contoured as a function of y and frequency. The modes are computed for 10 frequency bands between 0.043 and 0.43 cpd, the same frequencies and frequency bandwidth used for the autospectra in Fig. 8. The subdomains in y-frequency space dominated by the first two modes are sharply delineated by the contours of percent variance explained in Fig. 9. The first mode represents most of the ζ variance poleward of grid point 9 (near CCY), and the second mode represents most of the variance equatorward of point 9, consistent with the time domain EOFs. However, a substantial percentage of sea level variance along the northern British Columbia coast is also contained in the second mode, which is not observed in the second time domain EOF. For consistency, we refer to these frequency domain EOFs as northern and southern modes.

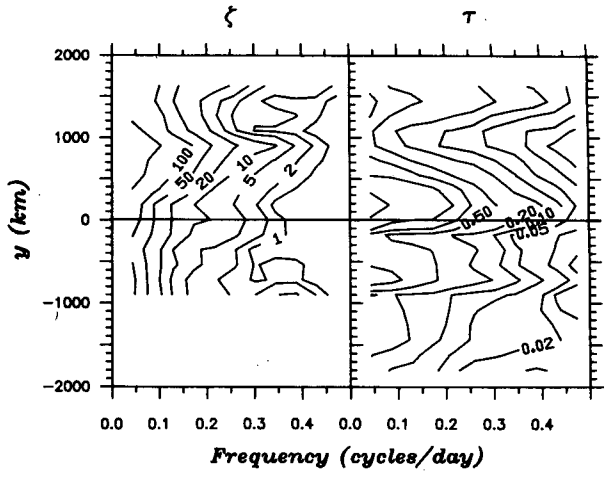

FIG. 8. Autospectra of ζ and calculated τ contoured as a function of frequency and y. The spectra are in units of cm^2 cpd^{-1} and (dyn cm^{-2})^2 cpd^{-1}, respectively. The frequency bandwidth is 0.043 cpd, resulting in 10 degrees of freedom.

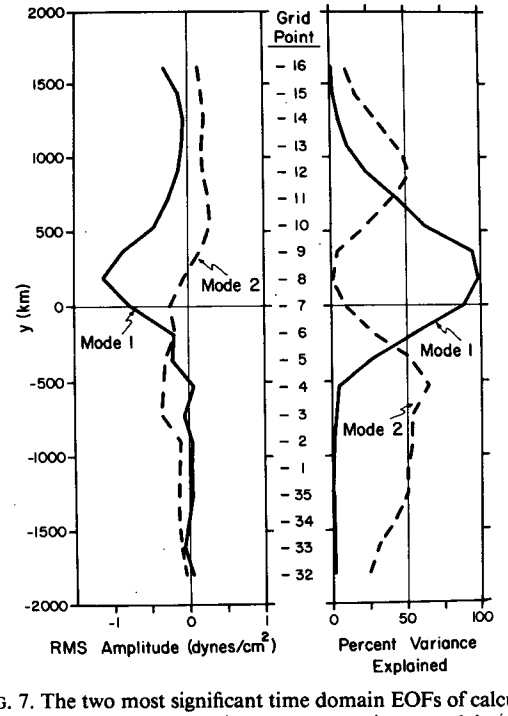

FIG. 7. The two most significant time domain EOFs of calculated τ: (left) rms amplitudes and (right) percent variance explained. The modes account for 66 and 17% of the total variance, respectively.

The plots of amplitude and percent variance explained show that the northern mode increases rapidly in amplitude poleward of $y = 0$ km. It has maximum amplitude along the southern Washington coast at a frequency of 0.086 cpd. The southern mode generally decreases in amplitude poleward of San Francisco, then increases again in amplitude along the northern British Columbia coast, and is therefore smaller in amplitude than the northern mode from Northern California through central British Columbia. The energy of the southern mode increases enough along the northern British Columbia coast to explain as much variance as the northern mode near Bella Bella.

From the contours of phase lag in hours, the northern mode fluctuations poleward of Cape Mendocino propagate poleward at roughly 600 cm s^{-1} between 0.086 and 0.17 cpd, a frequency band where the northern mode has relatively large amplitude. The northern mode extends equatorward along the central and southern California coast near 0.13 cpd based on the coherence with measured ζ, where the fluctuations propagate poleward at about 250 cm s^{-1}. At frequencies greater than 0.22 cpd, the phase lags are irregular and consistent phase propagation cannot be identified. The ζ fluctuations in the southern mode propagate poleward at roughly 250 cm s^{-1} for frequencies equal to or less than 0.086 cpd, a frequency band where the mode has

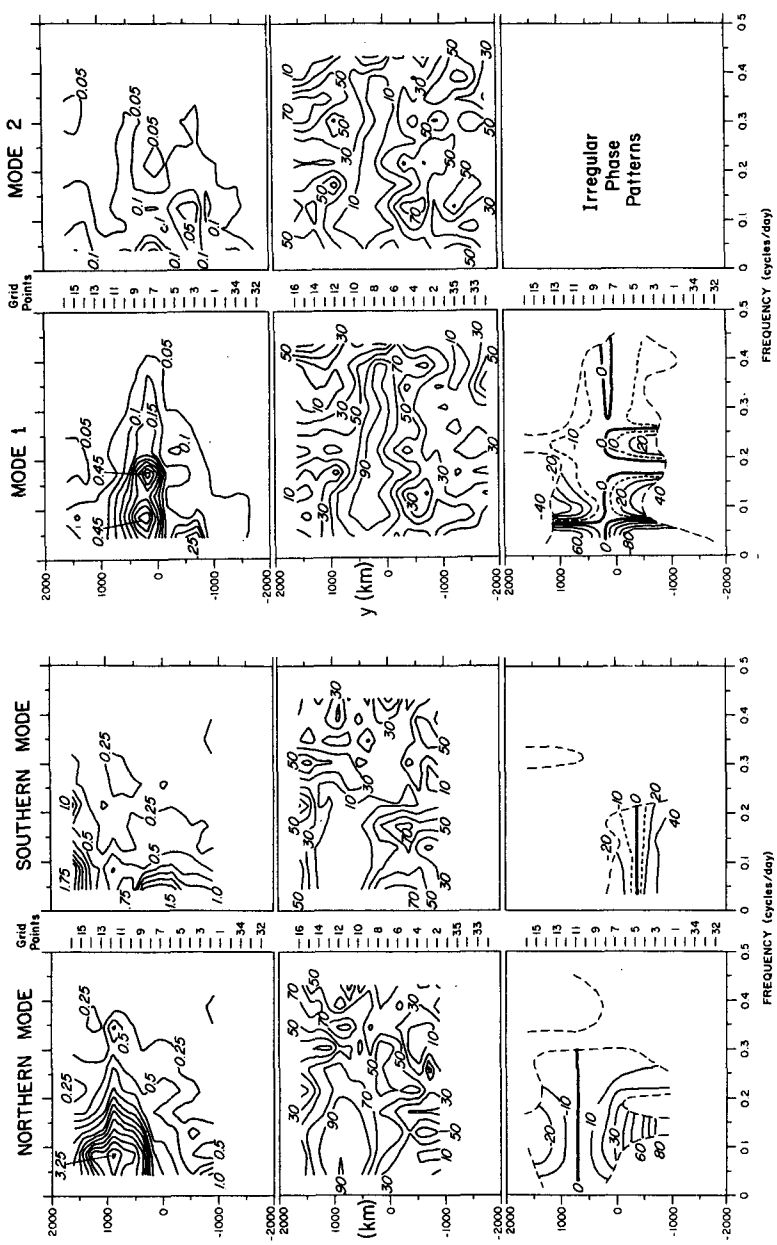

FIG. 9. The northern and southern frequency domain EOFs of gridded ζ contoured as a function of frequency and y: (top) rms amplitude in cm; (middle) percent variance explained; and (bottom) phase lag in h. The frequency bandwidth is 0.043 cpd, resulting in 10 degrees of freedom. Phase is contoured only over that part of the y-frequency domain where the coherence squared between the modes and gridded ζ is greater than 0.3. The y locations of the zero phase contours are the same over all frequencies for each mode and are arbitrarily chosen to be located near the middle of the alongshore subdomains where the modes are energetic.

FIG. 10. As in Fig. 9 for the two most significant frequency domain EOFs of calculated τ.

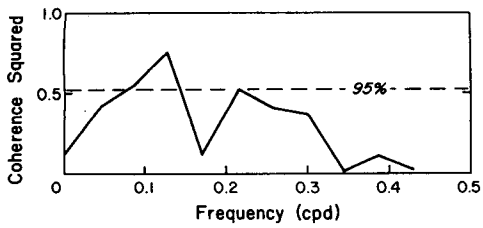

FIG. 11. Coherence squared between the northern frequency domain EOF of gridded ζ and the most significant frequency domain EOF of calculated τ. The frequency bandwidth is 0.043 cpd, resulting in 10 degrees of freedom. The 95% significance level is shown.

relatively large amplitude. The propagation speed increases to roughly 450 cm s^{-1} between 0.17 and 0.22 cpd, a frequency band where the mode has much smaller amplitude. Considering the properties of both modes, fluctuations in ζ poleward of Cape Mendocino tend to propagate substantially faster than fluctuations equatorward of the Cape.

Frequency domain EOFs of τ, calculated for the same frequency bandwidths as the ζ EOFs, are presented in Fig. 10. The most energetic mode represents the energetic fluctuations centered near Cape Mendocino plus some very low-frequency fluctuations located equatorward of the Cape and centered near Point Conception. The second mode is dominated by the relatively less energetic fluctuations located both poleward and equatorward of the Cape, consistent with the spatial structures of the first two time domain EOFs of τ (Fig. 7).

Phase contours of mode 1 display a banded structure over frequency. A band of equatorward propagating fluctuations exists at frequencies near 0.043 cpd. Poleward of Cape Mendocino, poleward propagation exists over all frequencies equal to or greater than 0.086 cpd. Equatorward of Cape Mendocino, poleward propagation exists in the frequency bands centered near 0.086, 0.13, and 0.22 cpd, with equatorward propagation in the frequency band centered near 0.17 cpd and over all frequencies greater than 0.22 cpd. Thus, propagation is exclusively poleward throughout the alongshore domain of the mode in the three frequency bands centered near 0.086, 0.13, and 0.22 cpd. The computed phase lags for τ mode 2 are irregular and consistent phase propagation cannot be identified.

We compute the coherence squared (Fig. 11) between the northern ζ mode and τ mode 1 using the method of Denbo and Allen (1984). The only coherences significant at the 95% level of confidence are observed at the same three frequencies (0.086, 0.13, and 0.22 cpd) where mode-1 τ fluctuations propagate exclusively poleward throughout the entire alongshore subdomain of the mode.

The largest amplitude of τ mode 1 is observed along the Oregon and northern California coast at two frequencies, 0.086 and 0.17 cpd. The largest amplitude of ζ mode 1 is observed along the Washington coast at 0.086 cpd, with no indication of a relative maximum near 0.17 cpd. At 0.086 cpd, the fluctuations in τ mode 1 propagate poleward at about 350 cm s^{-1} between Point Conception and Neah Bay. At 0.17 cpd, these fluctuations are nearly in-phase, implying very rapid alongshore propagation speeds (>1000 cm s^{-1}), with equatorward propagation south of Cape Mendocino. Thus, ζ mode 1 has its largest amplitude and is significantly coherent with τ mode 1 at the only frequency (0.086 cpd) where the τ mode has both a relative amplitude maximum and poleward propagation over its entire alongshore domain at a speed relatively close to the observed propagation speed of fluctuations in ζ. At 0.17 cpd, the τ mode only possesses the first

TABLE 6. Summary of the space and time lagged correlation analyses between ζ at each of six selected stations and τ at all grid points. Correlation maxima relative to each ζ station are numbered sequentially from north to south and are marked by the solid dots in Fig. 12. The y locations plus the space and time lags (Δy and Δt) of each maximum are given, from which a characteristic speed (with error estimates in parentheses based on a ±6 h uncertainty in lag time) is estimated.

ζ Station	No.	Correlation maxima	y (km)	Δy (km)	Δt (days)	$\Delta y/\Delta t$ (cm s^{-1})
BBL	1	0.48	720	−888	−3.00	340 (314–371)
NBA	1	0.68	540	−560	−1.75	368 (322–429)
	2	0.25	−1080	−2180	−5.75	436 (418–456)
SBC	1	0.79	540	−138	−0.75	212 (159–317)
	2	0.28	−1080	−1758	−4.75	426 (404–449)
CCY	1	0.68	−180	−539	−1.50	413 (354–495)
	2	0.49	−1080	−1439	−4.00	414 (389–441)
MRY	1	0.51	−360	−84	−1.00	97 (77–129)
	2	0.43	−900	−624	−3.00	239 (220–261)
LBC	1	0.45	−1260	−475	−0.50	1092 (728–2185)

property, and it is not significantly coherent with the ζ mode (Fig. 11). The response of ζ to fluctuations in τ is frequency-dependent, and at a given frequency it apparently depends on both the amplitude and alongshore propagation speed (hence the wavenumber) of the fluctuations in τ. Although it is not clearly demonstrated here, the response presumably also depends on the alongshore distance over which the τ field possesses these properties. Further studies using wavenumber–frequency decompositions of ζ and τ are in progress.

6. The relationship of sea level response to the large-scale wind stress field

Space- and time-lagged correlations between ζ at six stations from Bella Bella to Long Beach and calculated τ at all grid points are analyzed to study the alongshore variability of the response of ζ to τ. These ζ–τ correlations are contoured as a function of lag time and y in Fig. 12. It is evident that ζ tends to be more highly correlated with τ equatorward from, and earlier in time than, the location and time of the ζ measurements. These lags are estimated from Fig. 12 and summarized in Table 6. Correlations between τ at the six grid points closest to the six ζ stations used in the ζ–τ correlation analysis and τ at all grid points are contoured in Fig. 13, and correlations between ζ at these six grid points and ζ at all grid points are contoured in Fig. 14.

From the ζ–τ correlation patterns (Fig. 12), fluctuations in ζ at Bella Bella (BBL), Neah Bay (NBA), and Southbeach (SBC) are all most highly correlated with τ along the southern Oregon and extreme northern California coast. The lag times for these stations become more negative with increasing poleward separation from the northern forcing region, ranging from -0.75 days at SBC to -3.0 days at BBL. At BBL and NBA, the correlation of ζ with local τ is insignificant. The τ–τ correlation patterns relative to grid points 16 and 13 (Fig. 13) do not show a corresponding correlation peak at negative lag times along Northern California and Oregon. The ζ–ζ correlation patterns relative to grid points 16 and 13 (Fig. 14) show that ζ at these points is relatively well correlated with ζ along the Oregon coast, the apparent origin of much of the ζ energy observed at these grid points. Apparently, fluctuations in ζ along Washington and British Columbia are dominated by free wave energy that is forced along the Northern California and Oregon coast.

Near-local forcing is apparently much more important at SBC, where the ζ–τ correlation peak is located within 200 km equatorward of SBC. The corresponding τ–τ and ζ–ζ correlation patterns relative to grid point 11 both have positive slopes in the major axes of the central correlation peaks. The τ–τ correlation peak relative to grid point 9 (near CCY) also has positive slope. Positive slopes are expected if poleward propagating energy exceeds equatorward propagating energy. This indicates that near-resonant forcing may be relatively important along the Oregon and extreme northern California coast. In contrast, the central peaks of the τ–τ correlation patterns relative to grid points 16 and 13 do not have a noticeable slope, indicating that near-resonant forcing is less important along the Washington and British Columbia coast. This is probably one reason why near-local atmospheric forcing is not very important along this part of the coast.

The slopes of the ζ–ζ correlation peaks in Fig. 14 from grid point 9 to the south are substantially smaller than the slopes at the northern grid points, except at grid point 2 where a slope cannot be discerned. The slope relative to grid point 9 is smaller equatorward of the point than poleward of the point. This indicates that propagation speeds are smaller along the California coast than to the north, in agreement with the results of the frequency-domain EOF analysis.

The existence of the southern forcing region along the Northern Baja California coast (near $y = -1080$ km) is evident in the ζ–τ correlations from the statistically significant correlation maxima between ζ at CCY, MRY and Long Beach (LBC) and τ along Northern Baja California at negative lag times (Fig. 12). Effects of this forcing region appear as far poleward as NBA, since weak correlation maxima between τ near $y = -1080$ km and ζ at NBA and SBC are also observed at negative lag times in Fig. 12. These correlation maxima again occur at increasingly negative lag times with increasingly poleward separation of the ζ station from $y = -1080$ km (Table 6). However, part of the high correlation with τ near $y = -1080$ km may be due to correlation patterns in the τ field itself. At grid point 2, τ is relatively well correlated with τ at locations poleward of the grid point, giving a positive slope to the τ–τ correlation peak (Fig. 13). Thus, τ fluctuations along Northern Baja California appear to propagate poleward to Northern California.

A characteristic speed of forced ζ fluctuations may be estimated from the lag distances (Δy) and lag times (Δt) of the correlation maxima denoted by the solid dots in Fig. 12. A rough estimate of uncertainty is obtained by computing a range of speeds for a lag time uncertainty of ± 0.25 days. Most speed estimates range between 200 and 450 cm s^{-1}. The two exceptions are for the correlation maxima located within 100 km equatorward of MRY, where the speed is about 100 cm s^{-1}, and for the one correlation maximum located equatorward of LBC, where the speed is over 1000 cm s^{-1}.

We do not pursue a dynamical interpretation of these results here. The problem is addressed by Allen and Denbo (1984), who show that the space–time

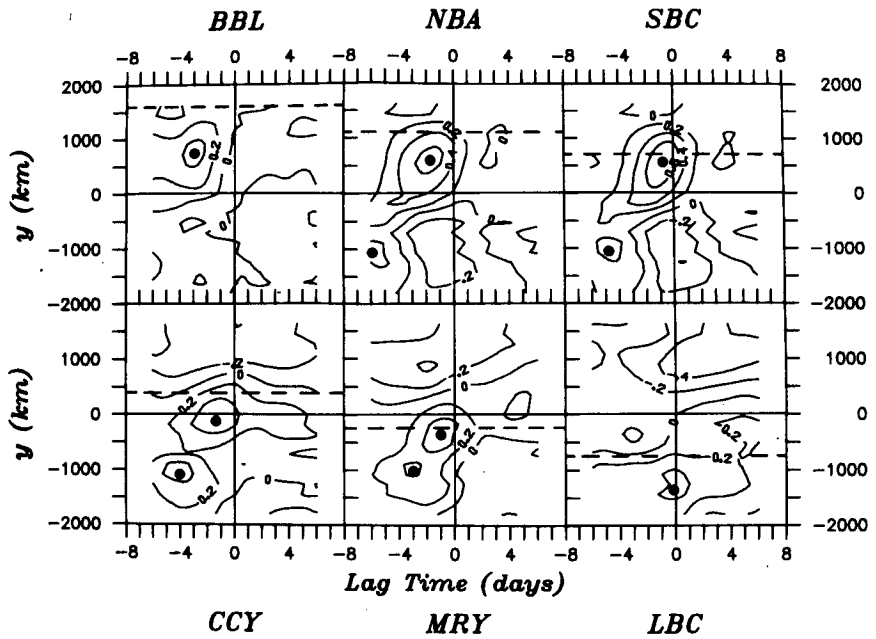

FIG. 12. Contours of the space and time lagged correlation of ζ at each of six selected measurement stations with calculated τ at all grid points. The alongshore locations of the ζ stations are shown by the horizontal dashed lines; therefore, the correlations are spatially lagged with respect to these lines. The alongshore locations and lag times of the correlation maxima at the two forcing regions are shown by the solid dots. Lag distances and lag times for these maxima are summarized in Table 6. The integral time scales (Davis, 1976) vary for different time series: in general, statistically significant cross-correlations between ζ and τ are ≥ 0.33 to a 95% level of confidence.

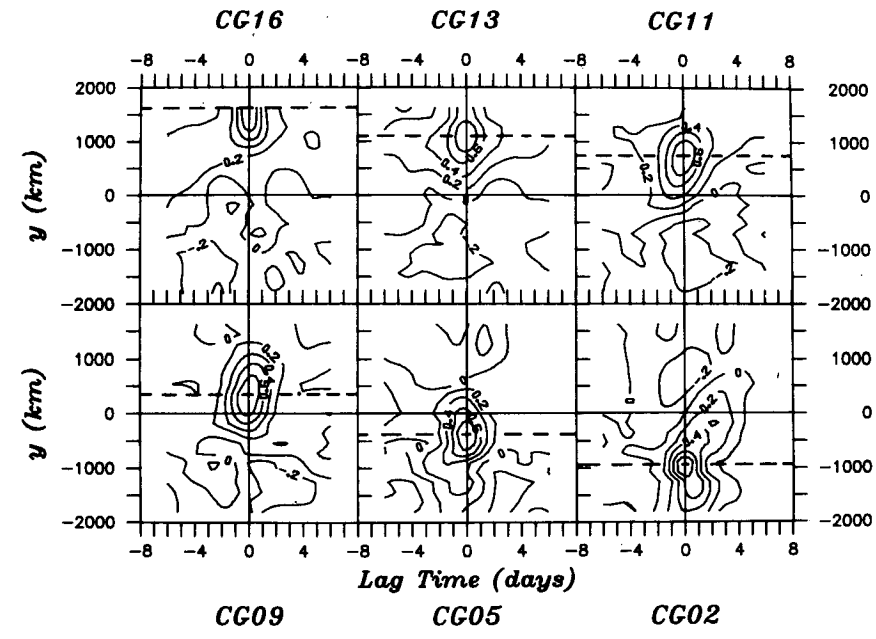

FIG. 13. Contours of the space and time lagged correlation of calculated τ at each of the six grid points nearest to the six ζ stations in Fig. 12 with calculated τ at all grid points. The alongshore locations of the grid points are shown by the horizontal dashed lines; therefore, the correlations are spatially lagged with respect to these lines. Statistically significant correlations are ≥ 0.32 to a 95% level of confidence.

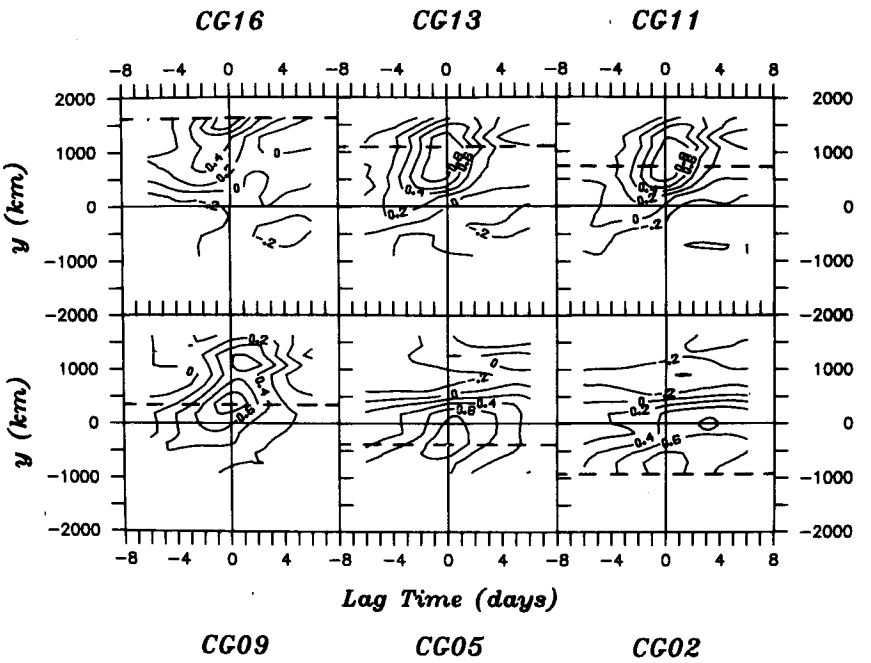

FIG. 14. As in Fig. 13 for gridded ζ. Statistically significant correlations are ≥ 0.38 equatorward of CCY and ≥ 0.32 poleward of CCY to a 95% level of confidence.

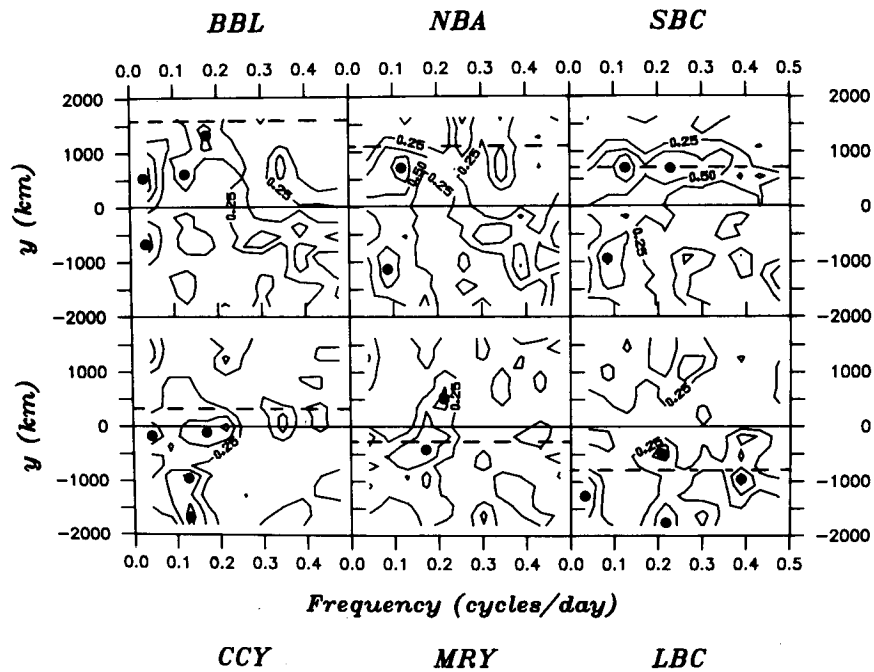

FIG. 15. Contours of the space lagged coherence squared of ζ at the six measurement stations used in the correlation analysis with calculated τ at all grid points. The alongshore locations of the ζ stations are shown by the horizontal dashed lines; therefore, the coherences are spatially lagged with respect to these lines. The alongshore locations and frequencies of the coherence maxima at the two forcing regions (see Fig. 12) are shown by the solid dots. The frequency bandwidth is 0.043 cpd, resulting in 10 degrees of freedom. Squared coherences of 0.52 are statistically significant to a 95% level of confidence. The contour interval is 0.25.

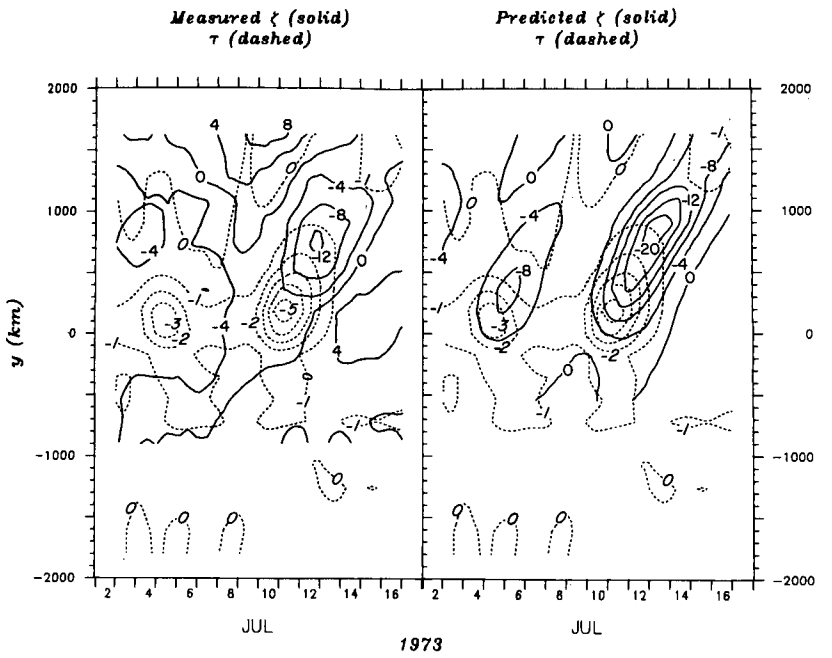

FIG. 16. Space-time contours of six-hourly calculated τ in dyn cm^{-2} (dashed) and six-hourly gridded ζ in cm (solid) for 3 July through 19 July 1973, spanning τ events 4 and 5. The observed ζ response to τ is shown on the left, and the response predicted by (7.2) is shown on the right.

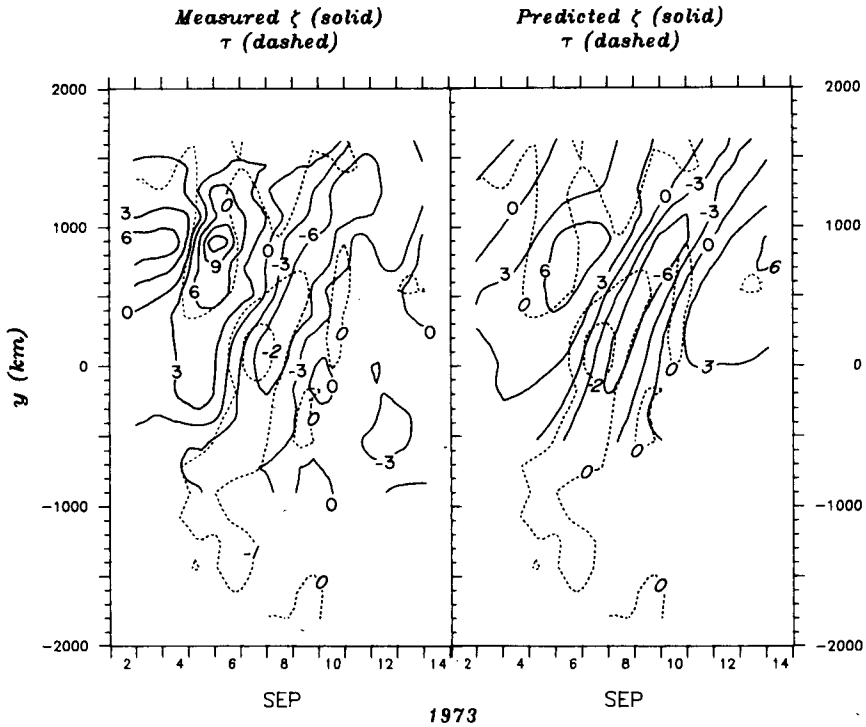

FIG. 17. As in Fig. 16, but for the time interval of 3–13 September 1973, spanning τ event 11. Also shown is a preceding τ event (not numbered in Fig. 3) which forced the large ζ maximum on 5 and 6 September.

lagged ζ–ζ and τ–τ correlation patterns observed here are implied by the first-order wave equation of Gill and Schumann (1974). This equation is discussed in Section 7.

The relationship of the ζ-response to the large-scale τ field is examined in the frequency domain by contouring squared coherences between ζ at six stations and τ at all grid points as a function of frequency and y (Fig. 15). The two forcing regions are evident in the τ–ζ coherence plots for BBL, NBA, and SBC. The coherence between SBC ζ and τ in the northern forcing region is large over a broad frequency band from 0.043 to about 0.4 cpd. The τ–ζ coherence patterns relative to NBA and BBL indicate that the coherent frequency band narrows and shifts toward very low frequencies (near 0.043 cpd relative to BBL ζ) with increasing alongshore separation from the northern forcing region. The coherence maximum between NBA and SBC ζ and τ in the southern forcing region is near 0.086 cpd, while the corresponding coherence maximum between BBL ζ and τ is near 0.043 cpd. Apparently, only the lowest-frequency component of the wind-forced ζ fluctuations from both forcing regions reaches BBL. At CCY and MRY, ζ is most coherent with τ between the alongshore locations of these stations and the southern end of the analysis domain for frequencies less than about 0.2 cpd. At LBC ζ is most coherent with τ along northern Baja California at a frequency of 0.043 cpd. A coherence maximum also exists between LBC ζ and τ at $y = -900$ km at a frequency of about 0.4 cpd. This indicates that the relatively large ζ energy observed near the southern end of the analysis domain at this frequency (Fig. 8) is probably wind-driven.

7. Dynamical interpretation of the observed response to wind stress forcing

To assess the dynamics of the ζ response to τ fluctuations, we focus on τ events 4 and 5 (Fig. 16) plus event 11 (Fig. 17) by overlaying contours of six-hourly τ and gridded ζ. We compare these observations to ζ predicted from the observed τ using a simple theoretical model. Events 4 and 5 are both pulses of strong equatorward τ, with the pulse associated with event 5 propagating poleward at about 500 cm s^{-1} and evidently capable of more effective forcing of ζ than event 4, which propagates equatorward at about 650 cm s^{-1}. Event 4 depresses ζ by less than 3 cm, with the response occurring later in time and poleward of the time line of the τ extremum (Fig. 16). Event 5 depresses ζ by up to 14 cm, more than four times greater than the response to event 4, even though the maximum amplitude of τ is only 1.5 times greater. The maximum response amplitude occurs at the poleward edge of the τ event.

Event 11 propagates poleward at about 550 cm s^{-1}, and it extends over a larger alongshore domain than the other events (Fig. 17). The resulting depression in ζ propagates poleward along with, but occurring about one-half day later than, the location and time of the τ extremum. A large ζ maximum forced along the Oregon coast about three days prior to event 11 is also observed in Fig. 17. A weak, poleward propagating (at about 700 cm s^{-1}) τ maximum is apparently responsible for this response.

In linear models of wind-forced coastal-trapped waves, if the variables are expanded in terms of modes dependent on the cross-shelf and vertical coordinates, the alongshore and time-dependent behavior $Y_n(y, t)$ of the nth mode is governed by a forced, first-order wave equation (Gill and Schumann, 1974, Clarke, 1977):

$$c_n^{-1} Y_{nt} + Y_{ny} + (c_n T_f)^{-1} Y_n = b_n \tau(y, t), \quad (7.1)$$

where the subscripts (y, t) denote partial differentiation, c_n is the free-wave phase speed of the nth mode, b_n a constant dependent on the mode structure and topography, and T_f the friction time scale. Free wave solutions to the homogeneous equation propagate toward $+y$ at speed c_n, or along the characteristic line in y–t space given by $y - c_n t =$ constant.

We assume that fluctuations in ζ are dominated by the lowest mode and drop the subscripts. We then compare the observed alongshore-time behavior of ζ to Y predicted by (7.1) using observed (calculated) $\tau(y, t)$ as the forcing function. The solution of (7.1) at y and t is an integral of wind stress along the characteristic through y, t weighted by an exponential function due to friction

$$Y = b \int_0^\infty \exp(-r/cT_f)\tau(y - r, t - r/c)dr. \quad (7.2)$$

The influence of τ equatorward of y decreases exponentially with increasing separation. We predict time series of ζ at the CODE analysis grid points by numerically integrating (7.2). This is similar to the procedures used by Hamon (1976), who tested (7.1) by predicting ζ at one location on the east coast of Australia, and Clarke (1977), who predicted ζ at Depoe Bay, Oregon for a 34 day period during summer 1972.

Numerical integrations of (7.2) are performed along the characteristics using constant c, T_f and b. Since the southern boundary of the τ grid (26°N) is considerably farther south than the southernmost ζ point (33°N), we approximate the infinite integral (7.2) for Y, which neglects an exponentially damped contribution from ζ at the southern boundary. The predicted time series of ζ begin at 0000 on 16 June, which provides sufficient time for the initial ζ distribution to propagate through the analysis domain. Predictions are made only for locations poleward of Point Conception ($y = -540$ km), since the southern boundary contribution will make the predictions relatively inaccurate equatorward of the point. Thus, the prediction

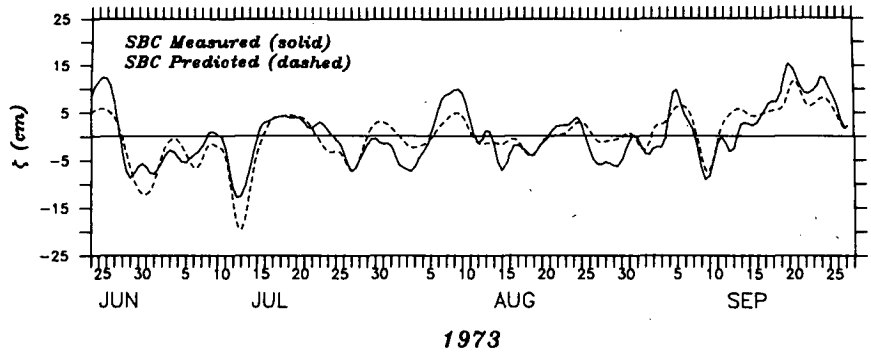

FIG. 18. Time series of measured and predicted ζ at SBC.

consists entirely of fluctuations forced within the study domain after 3 June.

We first estimate values of c, T_f, and b that give the best predictions of ζ within the most energetic alongshore subdomain of the wind-driven northern ζ mode, essentially the Washington and Oregon coast. To determine these parameters, trial predictions of ζ are made at four sea level stations: NBA, Toke Point (TKP), SBC, and Umpqua River (UMP), using different values of c and T_f in the range $250 \leq c \leq 400$ cm s^{-1} and $2.5 \leq T_f \leq 6.0$ days. The values of these parameters and of b that maximize the fraction of total variance explained by the prediction at these four stations are then determined. The best predictions, which explain 64% of the total variance at these stations, are obtained using $c = 325$ cm s^{-1}, $T_f = 4.25$ days, and $b = 1.19 \times 10^{-7}$ (dyn cm^{-2})$^{-1}$. These values are used in the subsequent analysis. This value of c is smaller than the observed phase speed of the northern ζ mode which dominates ζ fluctuations along Oregon and Washington. These phase speeds probably differ for several reasons:

1) observed ζ-fluctuations consist of both forced and free wave energy;
2) both observed phase speeds and theoretical free wave phase speeds are not constant along the coast;
3) more than one coastal-trapped wave mode may be present.

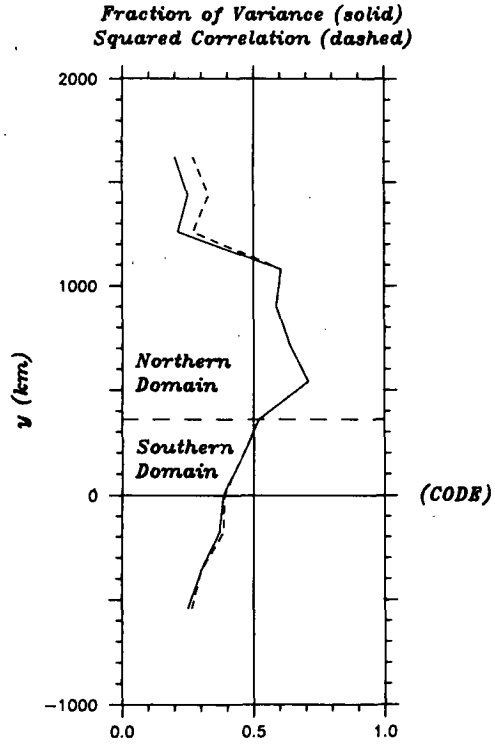

FIG. 19. The fraction of the total variance of gridded ζ explained by the prediction from (7.2) (solid line) and the squared correlation coefficients between measured and gridded ζ (dashed line). The squared correlation is greater than the fraction of variance explained because a single transfer coefficient b was obtained by maximizing total variance explained at four stations along the Oregon and Washington coasts.

The quality of these test predictions is not very sensitive to the parameter T_f, with the fraction of total variance explained changing by less than one percent for $2.5 \leq T_f \leq 6.0$ days at $c = 325$ cm s^{-1}. Squared correlation coefficients between ζ predicted at these four stations and ζ at SDO are no larger than 0.023, indicating that the neglect of ζ fluctuations propagating into the analysis domain through the southern boundary does not significantly effect the prediction of ζ poleward of the northern forcing region.

The quality of predicted ζ at SBC may be seen in Fig. 18. The zero-lag correlation coefficient between the measured and predicted time series is 0.83, while the zero-lag correlation between measured ζ and local τ is 0.72.

We determine the quality of the prediction poleward of Point Conception by computing the fraction of the variance of measured ζ explained by predicted ζ at each station (Fig. 19). Between Cape Mendocino and Point Conception ($0 > y > -540$ km) and along most of the British Columbia coast ($y > 1200$ km), less than half of the variance is explained by the prediction. In between, up to 70% of the variance is explained by the prediction. The higher quality of the prediction

along the Washington and Oregon coast occurs partly because we used constant values of c, T_f and b set to give the best prediction for this segment of the coast, and partly because it is located north of the strongest forcing region. However, the prediction does explain a larger fraction of the ζ variance at all locations than local τ alone.

Predicted ζ is contoured along with calculated τ for the selected τ events in Figs. 16 and 17. The predicted ζ responses to these four events are qualitatively very similar to the observed responses. Wind stress event 4 has a much smaller predicted ζ response than event 5 (Fig. 16), smaller than would be expected by just considering the smaller amplitude of τ event 4. This is expected theoretically since the τ extremum associated with event 5 propagates poleward at about 500 cm s^{-1}, and should more effectively force ζ fluctuations than event 4, which propagates equatorward. The predicted ζ maximum for event 5 occurs at the poleward edge of the event, as did the measured ζ maximum, although the measured amplitude is somewhat smaller. The predicted ζ responses to the two τ events in Fig. 18 are very similar to the measured responses, although the predicted response to the first event is smaller in amplitude than the measured response.

Differences in the measured and predicted amplitudes of ζ cannot be considered critical, since they may be due to alongshore variations in the coefficient b or to errors in the calculated wind field. The choice of 325 cm s^{-1} for the phase speed may have maximized the percent variance explained by the prediction along the Oregon and Washington coast, but the ζ response to individual events did not always propagate poleward at that speed. For example, the response to event 5 propagates poleward at about 500 cm s^{-1}.

We conclude that the first-order, forced coastal-trapped wave dynamics provide a fairly good description of the observed ζ fluctuations. The errors in predicted ζ can be attributed to several possible factors. In addition to the three factors listed earlier to explain the differences between c and the observed phase speeds, these are:

1) the parameters T_f and b are not constant along the coast;

2) the parameters c, T_f, and b depend on factors such as stratification and may be variable in time;

3) imperfect winds are used to represent the wind stress forcing function;

4) noise and local geographical effects affect measured ζ;

5) dynamical processes other than wind-forced large-scale coastal-trapped waves may influence ζ fluctuations.

8. Discussion

During summer 1973, the dynamics of large-scale coastal-trapped waves explained a large fraction of the observed ζ variance along the coast from northern Baja California to British Columbia. Atmospheric forcing was not uniform along the coast, and the most effective forcing was confined primarily to two regions. The northern California and Oregon coast was the region of strongest forcing, while northern Baja California was a region of significant but weaker forcing. The forced fluctuation of ζ propagated poleward from these forcing regions. Local forcing was so weak along the British Columbia coast that ζ fluctuations were apparently dominated by free wave energy propagating poleward from the northern forcing region. Fluctuations forced in the southern region were detectable poleward to northern Washington.

Forcing within the northern region was very strong for two reasons: first, the strongest τ fluctuations existed along the Northern California coast; and second, poleward propagating fluctuations in τ were apparently more energetic than equatorward propagating fluctuations. The variance of τ was an order of magnitude larger near Cape Mendocino than at locations more than a few hundred kilometers poleward and equatorward of the Cape. We also observed that poleward propagating τ events more effectively forced ζ fluctuations than equatorward propagating events. Since most of the τ variance in the northern forcing region was uncorrelated with τ at other locations, forced fluctuations of ζ both within and poleward of this forcing region were poorly correlated with fluctuations of ζ equatorward of the region. Most of the ζ variance was therefore explained by two EOFs in both the time and frequency domains, each dominating the ζ fluctuations along different segments of the coast, with the dividing zone located near CCY. The dividing zone was not an insurmountable barrier, since ζ fluctuations driven along Northern Baja California could still be weakly detected along the Oregon and Washington coast. The northern forcing zone was so effective that ζ fluctuations poleward of CCY that were driven in this zone strongly dominated the ζ fluctuations from the southern forcing region that propagated poleward past CCY.

The northern ζ fluctuations propagated poleward at about 600 cm s^{-1}, and the southern ζ fluctuations propagated poleward at about half that speed in the most energetic frequency bands. Observed wavelengths were greater than 1000 km along the entire coast, and the most energetic fluctuations had wavelengths greater than 2000 km. A frequency domain EOF representing the northern ζ fluctuations had an amplitude maximum near 0.086 cpd, and a frequency domain EOF representing the southern ζ fluctuations had an amplitude maximum at lower frequencies. A period equal to or greater than four months was visually evident in the amplitude time series of the corresponding southern time domain EOF.

We observed that ζ fluctuations at a given location y along the coast are most highly correlated with τ earlier in time and equatorward of y, with the space

and time lags dependent on location, since the effectiveness of τ forcing was not uniform along the coast. If y was located within a forcing region, the lags ranged from 100 to 500 km equatorward of y and 1 to 2 days earlier in time. If y was located away from a forcing region, both lags were larger. For example, ζ at BBA was most highly correlated with τ along the Oregon coast (about 900 km equatorward of BBA) about 3 days earlier in time. Knowledge of large-scale processes can therefore be important to shelf circulation studies in determining how ζ, and therefore currents, are driven by τ. Wind stress data should be collected more than 1000 km away from the study region in the direction from which coastal-trapped waves propagate to be sure that important forcing regions, and the ζ fluctuations forced in those regions, are included in the analyses.

During the summer of 1973, τ calculated from FNOC pressure fields was as well correlated with ζ as the best available measured τ. Therefore, calculated τ proved to be a satisfactory forcing function for the purposes of this study. The calculated τ vector series were not aligned with measured τ along the entire alongshore domain except near Point Conception, and had to be rotated additionally an average of 50 degrees counterclockwise to correct this misalignment. This correction also approximately maximized the correlation between the alongshore component of τ and ζ, and therefore improved the quality of the results obtained in this study. Whenever calculated winds or wind stress are to be used in a study along the west coast of North America (and probably other regions as well), tests of the alignment of these winds should be conducted and the vector winds rotated if necessary.

Acknowledgments. This research was supported by the Oceanography Section of the National Science Foundation under Grant OCE-8014939 as part of the Coastal Ocean Dynamics Experiment (CODE). We thank Dr. D. B. Chelton, Dr. K. H. Brink, Dr. W. Crawford, and an anonymous referee for helpful comments.

APPENDIX A

The Large-Scale Relationship of CUE-II Currents to Calculated τ

In order to study the response of coastal circulation to large-scale wind forcing over an alongshore domain sufficiently large to resolve the structure of both the forcing and the response, coastal sea level must presently be used as the response variable. Earlier studies of currents along the Pacific Northwest coast, such as those of Smith (1974), Kundu *et al.* (1975), and Huyer *et al.* (1978) determined that alongshore currents v and empirical modes of v are very well correlated with ζ (typically ≥ 0.8 during summer), presumably due to the approximate geostrophic balance of v (*e.g.*, Allen, 1980). These results strongly support the use of ζ as a proxy variable for v. Nevertheless, the question remains whether v has the same statistical relationship as ζ with the large-scale τ forcing field.

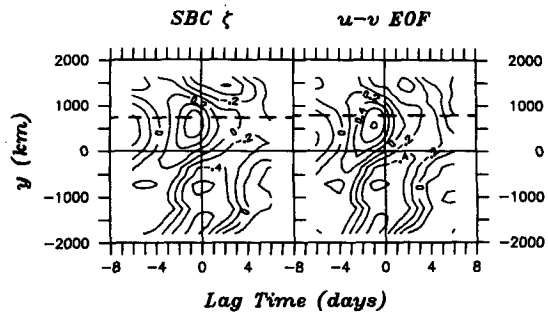

FIG. 20. Contours of the space and time lagged correlations of (left) ζ at SBC with calculated τ at all grid points and (right) the most significant u–v column time-domain EOF of currents at the CUE-II cross-shelf array discussed by Huyer *et al.* (1978) with calculated τ at all grid points. The alongshore locations of SBC and the current meter array are shown by the horizontal dashed lines; therefore, the correlations are spatially lagged with respect to these lines. The time interval for these calculations is 1800 PST 25 July 1973 to 1200 PST 25 August 1973. Since integral correlation time scales vary for different time series, a correlation coefficient of approximately 0.7 is statistically significant to a 95% level of confidence.

We therefore utilize the CUE-II current measurements off Oregon to test if v and ζ have the same statistical relationship with large-scale τ, first by inspecting the space and time lagged correlation patterns of both v and ζ with the calculated τ field, and second by comparing the quality of v and ζ predictions using (7.2). To represent the alongshore current, we use the amplitude time series of the most significant u and v column EOF of 11 current meters in the CUE-II cross-shelf array as presented by Huyer *et al.* This EOF is computed for a one-month time interval (the maximum time of overlapping current measurements) from 1800 PST 25 July to 1200 PST 25 August 1973. It explains 72% of the total variance and has a maximum correlation coefficient with SBC ζ of 0.86.

Space and time lagged correlations of both SBC ζ and the CUE-II current EOF with calculated τ at all grid points along the coast for the one-month time interval (Fig. 20) show a striking similarity in the patterns. The one-month correlation pattern for SBC ζ is also similar to the four-month pattern for SBC ζ (Fig. 12, upper right panel), at least in the structure of the primary correlation peak. The maximum correlation between SBC ζ and τ is 0.75 for the one-month period and 0.79 for the four-month period. The maximum correlation between the current EOF and τ is 0.82, substantially greater than the maximum of 0.75 for SBC ζ, which indicates that the current EOF has primarily extracted the large-scale, wind-driven signal contained in the current data. This dominant current signal has an almost identical relationship to the large-scale τ field as ζ.

A prediction of ζ from (7.2) also represents a prediction of the time variability of the alongshore current v. Therefore, cross-correlation analysis between a prediction and both ζ and v can be used to determine if v is predicted as well as ζ. To perform this comparison,

we use measured and predicted ζ at CG11 (Section 7), plus the amplitude of the CUE-II current EOF to represent the alongshore current. The zero-lag correlation is 0.78 between the prediction and ζ at CG11, and 0.87 between the prediction and the current mode. The higher correlation of the current mode is probably due again to the extraction of the large-scale, wind-driven signal by the EOF analysis. Most important, a prediction of the time variability of the first EOF of CUE-II currents is as good or better than the prediction of ζ, indicating that at this location the assumption of one wave mode is also useful for the prediction of v.

APPENDIX B

The Large-Scale Relationship of ζ to Measured τ

Here we test if the statistical relationship between ζ and the large-scale τ field is adequately determined

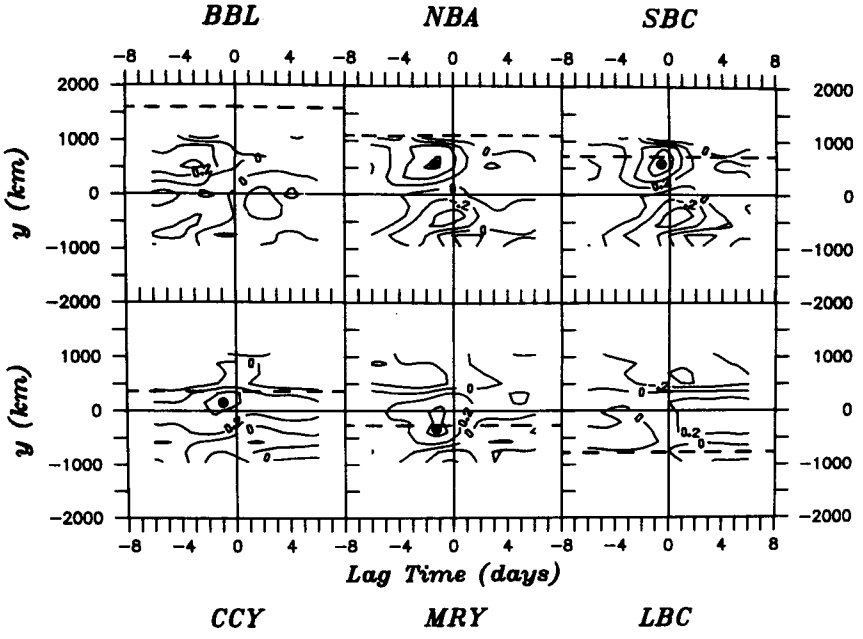

FIG. 21. As in Fig. 12 using measured τ at each of the 12 stations indicated in Table 1.

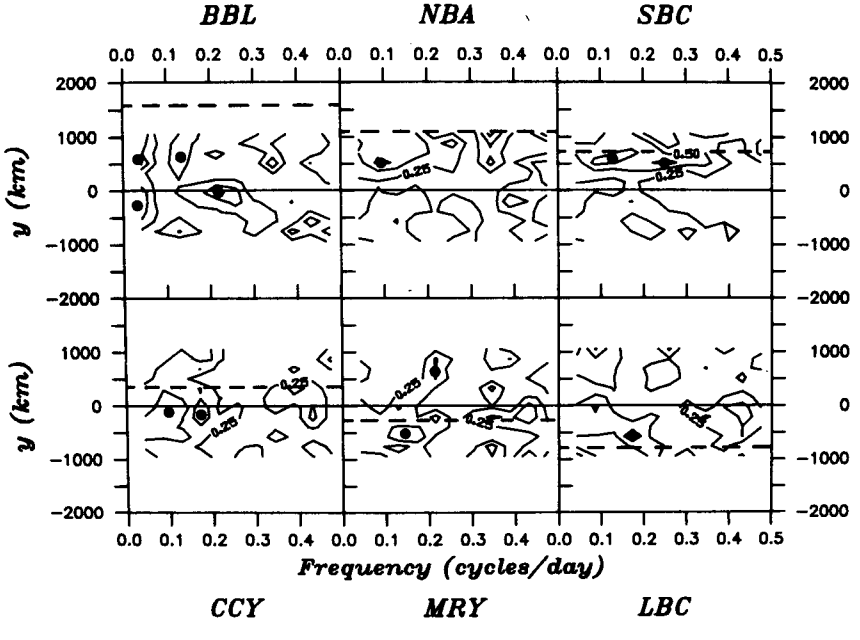

FIG. 22. As in Fig. 15 using measured τ at each of the 12 stations indicated in Table 1.

when calculated τ is used to represent this forcing. The correlation and coherence analyses in Figs. 12 and 15 are reproduced in Figs. 21 and 22 using measured τ at the 12 stations listed in Table 1. The analyses with measured τ are restricted to a smaller alongshore domain than the analyses with calculated τ since no measured winds are available off British Columbia or Baja California.

The correlation patterns between ζ and measured τ (Fig. 21) are very similar to the patterns between ζ and calculated τ (Fig. 12), except that the Northern Baja California forcing region is not detected because of the lack of good measured winds in that region. The maximum correlation for BBL ζ is the same (0.48) with both measured and calculated τ. For the other five stations, the maximum correlation of ζ with calculated τ is slightly larger than with measured τ. The corresponding squared coherences with measured τ (Fig. 22) also have similar patterns to the squared coherences with calculated τ (Fig. 15). We therefore conclude that calculated τ is adequately representative of the large-scale forcing for the purposes of this study.

REFERENCES

Allen, J. S., 1980: Models of wind-driven currents on the continental shelf. *Annual Reviews in Fluid Mechanics,* Vol. 12, Annual Reviews, 389–433.

——, and D. W. Denbo, 1984: Statistical characteristics of the large-scale response of coastal sea level to atmospheric forcing. *J. Phys. Oceanogr.,* **14,** 1079–1094.

——, R. Beardsley, W. Brown, D. Cacchione, R. Davis, D. Drake, C. Friehe, W. Grant, A. Huyer, J. Irish, M. Janopaul, A. Williams and C. Winant, 1983: Coastal Ocean Dynamics Experiment (CODE), a preliminary program description. *EOS,* **64,** 538–539.

Bakun, A., 1973: Coastal upwelling indices, west coast of North America, 1946–71. NOAA Tech. Rep. SSRF-671, National Marine Fisheries Service, Seattle, WA, 103 pp.

Chelton, D. B., and R. E. Davis, 1982: Monthly mean sea level variability along the west coast of North America. *J. Phys. Oceanogr.,* **12,** 757–784.

Clarke, A. J., 1977: Observational and numerical evidence for wind-forced coastal trapped long waves. *J. Phys. Oceanogr.,* **7,** 231–247.

Davis, R. E., 1976: Predictability of sea surface temperature and sea level pressure anomalies over the North Pacific Ocean. *J. Phys. Oceanogr.,* **6,** 249–266.

Denbo, D. W., and J. S. Allen, 1984: Rotary empirical orthogonal function analysis of currents near the Oregon coast. *J. Phys. Oceanogr.,* **14,** 35–46.

Enfield, D. B., and J. S. Allen, 1980: On the structure and dynamics of monthly mean sea level anomalies along the Pacific coast of North and South America. *J. Phys. Oceanogr.,* **10,** 557–578.

Garrett, C., and B. Toulany, 1982: Sea level variability due to meteorological forcing in the northeast Gulf of St. Lawrence. *J. Geophys. Res.,* **87,** 1968–1978.

Gill, A. E., and E. H. Schumann, 1974: The generation of long shelf waves by the wind. *J. Phys. Oceanogr.,* **4,** 83–90.

Halliwell, G. R., Jr., and J. S. Allen, 1983: CODE I: Large scale wind and sea level observations. CODE-I: Moored array and large scale data report, R. C. Beardsley and L. K. Rosenfeld, Eds., *WHOI Tech. Rep. 82-83,* 139–185.

——, and ——, 1984: Quality evaluation of measured and analyzed coastal winds along the west coast of North America, 26°N to 54°N. In preparation.

Hamon, B. V., 1976: Generation of shelf waves on the East Australian Coast by wind stress. *Mem. Soc. R. Sci. Liege,* **Ser. 10,** 359–368.

Huyer, A., R. L. Smith and E. J. C. Sobey, 1978: Seasonal differences in low frequency current fluctuations over the Oregon continental shelf. *J. Geophys. Res.,* **83,** 5077–5089.

Kundu, P. K., 1976: Ekman veering observed near the ocean bottom. *J. Phys. Oceanogr.,* **6,** 238–242.

——, J. S. Allen and R. L. Smith, 1975: Modal decomposition of the velocity field near the Oregon coast. *J. Phys. Oceanogr.,* **5,** 683–704.

Large, W. G., and S. Pond, 1981: Open ocean flux measurements in moderate to strong winds. *J. Phys. Oceanogr.,* **11,** 324–336.

Osmer, S. R., and A. Huyer, 1978: Variations in the alongshore correlation of sea level along the west coast of North America. *J. Geophys. Res.,* **83,** 1921–1927.

Pittock, H. L., W. E. Gilbert, A. Huyer and R. L. Smith, 1982: Observations of sea level, wind and atmospheric pressure at Newport, Oregon, 1967–1980. Data Rep. 98, Oregon State University, 158 pp.

Smith, R. L., 1974: A description of current, wind, and sea level variations during coastal upwelling off the Oregon coast, July–August, 1972. *J. Geophys. Res.,* **79,** 435–443.

Thomson, R. E., 1983: A comparison between computed and measured oceanic winds near the British Columbia coast. *J. Geophys. Res.,* **88,** 2675–2683.

Wallace, J. M., and R. E. Dickinson, 1972: Empirical orthogonal representation of time series in the frequency domain. Part I: Theoretical consideration. *J. Appl. Meteor.,* **11,** 887–892.

Wang, D-P., and C. N. K. Mooers, 1977: Long coastal trapped waves off the coast of the United States, summer 1973. *J. Phys. Oceanogr.,* **7,** 856–864.